High-resolution three-dimensional macromolecular proton fraction mapping for quantitative neuroanatomical imaging of the rodent brain in ultra-high magnetic fields

Anna V. Naumova[1,2], **Andrey E. Akulov**[3], **Marina Yu. Khodanovich**[2], and **Vasily L. Yarnykh**[1,2,*]

[1]University of Washington, Department of Radiology, 850 Republican Street, Seattle, WA, USA

[2]National Research Tomsk State University, Research Institute of Biology and Biophysics, 36 Lenina Avenue, Tomsk, Russia

[3]Institute of Cytology and Genetics, The Siberian Branch of the Russian Academy of Sciences, 10 Lavrentyeva Avenue, Novosibirsk, Russia

Abstract

A well-known problem in ultra-high-field MRI is generation of high-resolution three-dimensional images for detailed characterization of white and gray matter anatomical structures. T_1-weighted imaging traditionally used for this purpose suffers from the loss of contrast between white and gray matter with an increase of magnetic field strength. Macromolecular proton fraction (MPF) mapping is a new method potentially capable to mitigate this problem due to strong myelin-based contrast and independence of this parameter of field strength. MPF is a key parameter determining the magnetization transfer effect in tissues and defined within the two-pool model as a relative amount of macromolecular protons involved into magnetization exchange with water protons. The objectives of this study were to characterize the two-pool model parameters in brain tissues in ultra-high magnetic fields and introduce fast high-field 3D MPF mapping as both anatomical and quantitative neuroimaging modality for small animal applications. In vivo imaging data were obtained from four adult male rats using an 11.7T animal MRI scanner. Comprehensive comparison of brain tissue contrast was performed for standard R_1 and T_2 maps and reconstructed from Z-spectroscopic images two-pool model parameter maps including MPF, cross-relaxation rate constant, and T_2 of pools. Additionally, high-resolution whole-brain 3D MPF maps were obtained with isotropic 170 μm voxel size using the single-point synthetic-reference method. MPF maps showed 3–6-fold increase in contrast between white and gray matter compared to other parameters. MPF measurements by the single-point synthetic reference method were in excellent agreement with the Z-spectroscopic method. MPF values in rat brain structures at 11.7T were similar to those at lower field strengths, thus confirming field independence of MPF. 3D MPF mapping provides a useful tool for neuroimaging in ultra-high magnetic fields enabling both

*Corresponding author: Vasily L. Yarnykh, Ph.D. Research Associate Professor, Department of Radiology, University of Washington, 850 Republican St., Room 255. Seattle, WA, 98109. Tel.: 1-206-616-0259. fax: 1-206-616-9354. yarnykh@uw.edu.

quantitative tissue characterization based on the myelin content and high-resolution neuroanatomical visualization with high contrast between white and gray matter.

Graphical abstract
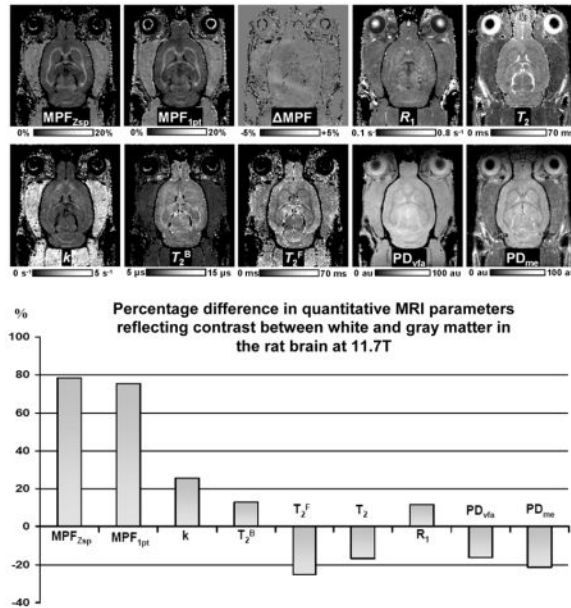
Keywords

High-field MRI; Macromolecular proton fraction (MPF); Neuroimaging; Rat brain

1. Introduction

An increase of magnetic field strength in MRI offers improvements of contrast in certain applications including functional, perfusion, and susceptibility-weighted imaging and a greater signal-to-noise ratio (SNR), which potentially can be converted into higher spatial resolution (Balchandani and Naidich, 2015; Lövblad et al., 2012; Ugurbil, 2014). However, imaging in ultra-high magnetic fields imposes a number of challenges, such as increased non-uniformity of B_0 and B_1 fields, larger specific absorption rate (SAR), more pronounced magnetic susceptibility artifacts, and changes in relaxation properties of tissues. A well-known problem in ultrahigh-field MRI is a decrease of T_1-weighted tissue contrast with an increase of field strength (Balchandani and Naidich, 2015; de Graaf et al., 2006; van de Ven et al., 2007; Pohmann et al., 2011; Kara et al., 2013). For this reason, T_2-weighted imaging remains the only suitable modality for routine neuroanatomical applications in magnetic fields beyond 9–10 T. However, high-field T_2-weighted imaging has some limitations in the morphological context. T_2-weighted images are typically acquired using a sequence with multiple spin-echo readout (RARE or FSE). T_2 shortening in high fields precludes using large acceleration factors in this sequence due to degradation of image quality caused by point spread function broadening. In combination with a long repetition time (TR) required for T_2-weighting, 3D T_2-weighted imaging with sufficiently high resolution in all directions

becomes prohibitively time-consuming for most small animal neuroimaging applications in vivo. Additionally, T_2-weighted imaging in high fields becomes very sensitive to the magnetic susceptibility effect caused by the presence of super-paramagnetic substances. This effect may result in obscuring anatomical details in cell labeling applications or in the presence of hemorrhage after surgical procedures. As such, small animal MRI in ultra-high magnetic fields is essentially lacking a technique that could afford high-resolution 3D visualization of brain morphology in vivo with minimal sensitivity to the susceptibility and paramagnetic effects and positive contrast between white matter (WM) and gray matter (GM).

One contrast mechanism that is potentially capable to mitigate contrast generation problems in ultra-high magnetic fields is the magnetization transfer (MT) effect. MT is frequently characterized by empirical semi-quantitative indexes describing changes in the signal intensity caused by radiofrequency saturation that is partially selective to the resonance of macromolecular protons. Examples of such indexes include MT ratio (MTR) (Dousset et al., 1992), MT saturation (MTsat) (Helms et al., 2008), and MTR difference observed in the recently proposed inhomogeneous MT experimental method (ihMTR) (Varma et al., 2015a). Some of these quantities, such as MTsat (Boretius et al., 2010) and ihMTR (Prevost et al., 2016) showed a promise in ultra-high field anatomical neuroimaging due to their capability to generate strong contrast between WM and GM on corresponding parametric maps. However, the above indexes are problematic to use for the objective quantitative characterization of pathological changes in tissues due to their complex dependence on the parameters of an imaging sequence and underlying biophysical model describing the MT effect. Alternatively, the MT effect can be characterized by a set of relaxation and cross-relaxation parameters defined within the two-pool model (Morrison and Henkelman, 1995). One parameter of this model describing a relative amount of immobile macromolecular protons involved into magnetization exchange with mobile water protons and termed below as the macromolecular proton fraction (MPF) is characterized by marked distinctions between WM and GM and strong associations with the myelin content established in a number of animal studies (Janve et al., 2013; Ou et al., 2009; Underhill et al., 2011; Samsonov et al., 2012; Thiessen et al., 2013). However, application of MPF maps for the purpose of structural neuroimaging is challenging, because their reconstruction typically involves multi-parameter fit procedures that require a large number of source images and are prone to substantial parameter uncertainties. This limitation has been overcome by the recent fast single-point MPF mapping method, which has enabled reconstruction of MPF maps in isolation from other two-pool model parameters based on a single MT-weighted image (Yarnykh, 2012; Yarnykh, 2016), thus facilitating clinically-targeted applications (Petrie et al., 2014; Yarnykh et al., 2015a; Yarnykh et al., 2015b). Latest human studies have demonstrated that MPF maps obtained using the single-point method are capable of generating very high contrast between WM and GM in the human brain at 3T and provide clinically relevant information about demyelination in both WM and GM (Petrie et al., 2014; Yarnykh et al., 2015a; Yarnykh, 2016). Using the recently developed variant of fast MPF mapping (Yarnykh, 2016), which requires only three source images, 3D MPF maps can be obtained with high spatial resolution, whole-brain coverage, and clinically acceptable scan time. The main theoretical advantage of MPF as a quantitative MRI parameter is its

independence of magnetic field strength. As such, one can expect that in high magnetic fields, MPF maps will provide not only a means for quantitative tissue characterization but also a useful modality for high-resolution neuroanatomical imaging.

While MPF itself is independent of magnetic field, such dependence may be expected for other parameters of the two-pool model. Since MPF measurements in the single-point method (Yarnykh, 2012) are based on constraining certain two-pool model parameters and their combinations, the corresponding constraints may be also field-dependent and need to be determined for specific field strengths. The objectives of this study were to characterize the two-pool model parameters in brain tissues in ultra-high magnetic fields and introduce fast high-field 3D MPF mapping as both anatomical and quantitative neuroimaging modality for small animal applications.

2. Materials and Methods

2.1. Image Acquisition

All described experiments have been carried out in accordance with the National Institutes of Health guide for the care and use of Laboratory animals. The experimental protocol was approved by the Bioethical Committee at the Institute of Cytology and Genetics (Siberian Branch, Russian Academy of Sciences). Four adult male Wistar rats were imaged under isoflurane anesthesia on a 11.7T horizontal-bore animal MRI scanner (BioSpec 117/16 USR; Bruker BioSpin, Ettlingen, Germany) with a four-channel surface phased-array coil. To obtain maps of the two-pool model parameters, a series of brain MT-weighted images at a variable offset frequency ( ) and effective flip angle (FA_{MT}) of the off-resonance saturation pulse (termed below Z-spectroscopic images) were acquired using a 3D MT-prepared spoiled gradient echo (GRE) sequence with TR/TE=25/2.7 ms and excitation flip angle α=9°. For off-resonance saturation, Gaussian pulse was used with duration 10 ms, 12 values in a range 0.75–48 kHz, and FA_{MT} = 500, 1000, and 1500°. Reference images for data normalization were acquired for each FA_{MT} at =100 kHz. Complementary $R_1=1/T_1$ maps were obtained using the variable flip angle (VFA) method with a 3D GRE sequence (TR/TE=25/2.7 ms, α=3, 12, 20, 25, 30°). To correct for field heterogeneities, 3D B_0 and B_1 maps were acquired using the dual-TE (TR/TE_1/TE_2 = 20/2.9/5.8 ms, α = 8°) (Skinner and Glover, 1997) and actual flip-angle imaging (AFI) (TR_1/TR_2/TE = 13/65/4 ms, α = 60° (Yarnykh, 2007) methods, respectively.

All images were acquired in the axial plane with whole-brain coverage and resolution of $200\times200\times445$ μm^3 (FOV = $34\times30\times16$ mm, matrix size $170\times150\times36$). Scan time for each Z-spectral and VFA data point was 1 min 41 s, and 1 min 48 s and 5 min 16 s for B_0 and B_1 mapping sequences, respectively Additionally, 2D T_2 mapping was performed with matched geometry and contiguous slices using multiple spin-echo sequence with TR=5 s and 16 echoes with 10 ms echo spacing (scan time 9 min 20 s).

To demonstrate the feasibility of high-resolution whole-brain MPF mapping, 3D MPF maps were obtained from three source images (MT-, PD-, and T1-weighted) with isotropic 170 μm^3 resolution (FOV = $34\times34\times34$ mm^3, matrix size $200\times200\times200$) using the single-point method with the synthetic reference image (Yarnykh, 2016). PD- and T_1-weighted GRE

images were acquired with TR/TE = 16/2.6 ms and α = 3° and 16°, respectively. MT-weighted images were acquired with TR/TE = 25/2.6 ms and α = 9°. Off-resonance saturation pulse was applied at the offset frequency 5 kHz with FA_{MT} = 500°. All images were obtained with three signal averages and the scan time of 24 min for the PD- and T_1-weighted scans and 37 min for the MT-weighted scan. In all 3D imaging experiments, linear phase-encoding order with 100 dummy scans, slab-selective excitation, and fractional (75%) k-space acquisition in the slab selection direction were used.

2.2. Image Reconstruction and Analysis

VFA R_1 and PD maps were reconstructed by fitting the Ernst equation with B_1 correction, similar to the earlier publications (Yarnykh, 2007; Yarnykh, 2012). Multiple spin-echo images were processed to yield T_2 and PD maps based on the three-parameter fit of the single-exponential model with the noise level as an adjustable parameter (Raya et al., 2010). Z-spectroscopic images after normalization to reference images obtained at =100 kHz and corresponding FA_{MT} along with R_1 maps were used to reconstruct maps of the four parameters of the two-pool model (MPF; rate constant for MT from free water to bound macromolecular protons, k; and T_2 of free and bound protons, T_2^F, and T_2^B) by fitting the pulsed steady-state matrix MT equation (Yarnykh, 2012) with the Super-Lorentzian absorption lineshape of the bound pool (Morrison and Henkelman, 1995). For Z-spectroscopic data processing, nominal offset frequencies and flip angles (FA_{MT} and α) were corrected in each voxel using B_0 and B_1 maps, as previously described (Yarnykh, 2012).

The single-point MPF map reconstruction algorithm was implemented in the recent modification with the synthetic reference image (Yarnykh, 2016). In this algorithm, a reference image for MT data normalization is computed from R_1, PD, and B_1 maps, and an MPF map is reconstructed using a single MT-weighted image normalized to the synthetic reference image and an R_1 map by iterative solution of the pulsed steady-state matrix MT equation with B_0 and B_1 corrections as described earlier (Yarnykh, 2012). The MT-weighted image obtained at = 5 kHz and FA_{MT} = 500° was used to compare MPF maps obtained by the single-point reconstruction method and four-parameter fit of the pulsed MT model. All reconstruction procedures were performed using custom-written C-language software.

Parameter measurements were performed in regions-of-interest (ROIs) on corresponding maps for a series of WM (cingulum, corpus callosum, external capsule, internal capsule, fornix, cerebellar WM) and GM (olfactory bulb, caudate putamen, hippocampus, superior colliculus, inferior colliculus, cerebellar GM, motor cortex, visual cortex, thalamus) structures using publically available ImageJ software (National Institutes of Health, Bethesda, MD, USA). Mean parameter values were calculated in ROIs centered at corresponding brain structures identified on MPF maps from 3–5 adjacent slices (depending on the structure size) and averaged bilaterally when applicable. MPF maps were chosen for definition of anatomic structures due to the highest contrast between WM and GM available for this imaging modality, as detailed below. The constrained parameter values for the single-point MPF determination (rate constant for MT from bound to free protons R=k(1−MPF)/MPF, T_2^B, and product $R_1 T_2^F$ (Yarnykh, 2012)) were calculated from the

primary fitted parameters (MPF, k, T_2^F, T_2^B, and R_1) measured in ROIs on corresponding maps for each anatomical structure and then averaged.

2.3. Statistical Methods

Mean and standard deviations (SD) of measured relaxation and cross-relaxation parameters were calculated for each anatomic structure. Bland-Altman analysis of pooled measurements across animals and anatomic regions was used to assess agreement between MPF estimates obtained from the four-parameter fit and single-point reconstruction. Significance of the bias was determined using the one-sample t-test for the differences between paired measurements. Linear regression was used to characterize the strength of correlation between mean MPF measurements obtained by the two methods across anatomic structures. Contrast between WM and GM was characterized by the percentage difference between parameters averaged across corresponding anatomic structures. Statistical significance was defined as $P<0.05$, and two-tailed tests were used in all analyses. All data are presented as mean ± SD. All statistical analysis was carried out in SPSS software (SPSS Inc, Chicago, IL, USA).

3. Results

Representative experimental and fitted Z-spectra from ROIs corresponding to the WM (corpus callosum) and GM (visual cortex) of a single animal are presented in the Fig. 1. The fitted curves and the experimental data obtained at various offset frequencies and nominal flip angles of the saturation pulse are in good overall agreement suggesting adequateness of the two-pool model. Examples of maps of the cross-relaxation parameters reconstructed from Z-spectroscopic images, an MPF map reconstructed by the single-point method, maps of relaxation parameter R_1 and T_2, and PD maps obtained from VFA (PD_{vfa}) and multi-echo (PD_{me}) images are illustrated in Figure 2. Brain anatomic structures identified on MPF maps are shown in Figure 3, and the corresponding mean values of relaxation and cross-relaxation parameters measured in ROIs are listed in Table 1. Based on measurements in ROIs, the mean constrained parameter values for the single-point MPF mapping method were determined as follows: R = 23 ± 6 s^{-1}, $R_1T_2^F$ = 0.013 ± 0.003, and T_2^B =10.3 ± 0.8 μs.

The bar graph of the percentage differences between average parameter values in WM and GM (calculated as 100(WM-GM)/GM) reflecting the capability of different parameters to generate brain tissue contrast is presented in Fig. 4. MPF maps reconstructed by both the full two-pool model parameter fit and the single-point method demonstrated high positive contrast between WM and GM allowing clear definition of anatomical structures (Figs. 2 and 3). Quantitatively, MPF enabled the largest difference between WM and GM being on the order of 75–80%, while other parameters showed relatively weak positive (k, R_1, and T_2^B) or negative (T_2^F, T_2, and PD) contrast with percentage differences not exceeding 25% (Fig. 4). Notably, R_1 maps obtained at 11.7T demonstrated particularly weak positive contrast that was almost similar in absolute values to the negative contrast seen on the PD_{vfa} maps (Figs. 2 and 4). This observation explains the loss of contrast between WM and GM on T_1-weighted images in ultra-high fields, as the two above image contrast sources cancel each other. On the other hand, the synergistic effect of moderate negative WM-GM contrast

provided by T_2 and PD terms explains the typical high-contrast appearance of brain structures on routinely used in ultra-high fields T_2-weighted images.

MPF maps reconstructed by the four-parameter fit of Z-spectroscopic images and the single-point method (Fig. 2) demonstrated very similar visual appearance. Their difference image (Fig. 2) does not indicate any tissue-dependent patterns and shows only minor low-frequency variations, which may be associated with field instability during acquisition or sub-voxel motion propagation in the slab-selection direction. The Bland-Altman plot of MPF measurements pooled across animals and anatomic structures (Fig. 5a) indicates the absence of significant bias (mean difference = 0.14±0.68%, P=0.06) and systematic variations of the error. Excellent agreement between both methods was further confirmed by the regression analysis of mean MPF measurements in anatomic structures (Fig. 5b), which demonstrated strong correlation (Pearson's correlation coefficient r=0.99, P<0.001) and non-significant intercept of the regression line (–0.4%, 95% confidence intervals: –1.0 – 0.2%, P=0.15).

Figure 6 illustrates the application of fast MPF mapping for high-resolution 3D neuroanatomical imaging in ultra-high magnetic fields in vivo. In this example, extremely clear visualization of anatomical details was achieved with isotropic voxel size of 170 μm and an acceptable for high-resolution animal experiments total scan time of 1.5 hours. The full 3D dataset was submitted to the Data in Brief journal (Naumova et al., submitted).

4. Discussion

The key finding of this study is the evidence of the fact that MPF provides the highest brain tissue contrast in ultra-high magnetic fields, whereas other relaxation and cross-relaxation parameters have limited capabilities of image contrast generation. Opposed to lower fields, a small relative difference between T_1 relaxation times in ultra-high fields precludes achieving sufficient contrast between WM and GM in T_1-weighted imaging, as demonstrated by our results and earlier studies (de Graaf et al., 2006; van de Ven et al., 2007; Pohmann et al., 2011; Kara et al., 2013). Furthermore, a weak positive contrast based on R_1 differences is offset by negative contrast due to differences in proton density, thus making impossible consistent visualization of tiny WM structures in the rodent brain using T_1-weighted imaging. A simple fast single-point MPF mapping method (Yarnykh, 2016) fully exploits the benefits of MPF as a source of brain tissue contrast while enabling routine applications in ultra-high magnetic fields with a reasonable acquisition time, high spatial resolution, and robust reconstruction.

MPF values in WM and GM structures measured by both Z-spectroscopic and single-point techniques in this study are in excellent agreement with earlier animal data obtained at lower field strengths (Stanisz et al., 2005; Underhill et al., 2011; Samsonov et al., 2012). Particularly, in the normal rat brain in vivo (Underhill et al., 2011) at 3T, MPF were in the ranges 11.3–13.9% for WM and 5.7–7.3% for GM, which are very close to our data. Similar values were reported at 3T for fresh bovine brain tissues ex vivo (13.9% for WM and 5.0% for GM (Stanisz et al., 2005)) and canine brain in vivo (12.1% for WM and 5.4% for GM (Samsonov et al., 2012)). In ultra-high field of 16.4T (Pohmann et al., 2011), averaged MPF

values across anatomic structures of the rat brain were also close to the values obtained in this study (10.8% in WM and 5.4% in GM). Our data appear in reasonable agreement with MPF measurements in the normal murine brain at 7T (Thiessen et al., 2013) (10% in the corpus callosum and 6.7% in cortex) and rat brain at 9.4T (Xu et al., 2014) (14.8% in WM and in 8.4% in GM as recalculated from the originally reported pool size ratio, a related measure of the macromolecular proton content), while slight positive or negative discrepancies can be attributed to distinctions in the measurement methodologies. MPF estimates in WM and GM of the human brain in vivo obtained at field strengths ranging from 0.5T to 7T based on multiple sources (Sled and Pike, 2001; Yarnykh, 2002; Ropele et al., 2003; Yarnykh and Yuan, 2004; Sled et al., 2004; Gloor et al., 2008; Underhill et al., 2009; Levesque et al., 2010; Dortch et al., 2011; Yarnykh, 2012; Dortch et al., 2013; Mossahebi et al., 2014; Petrie et al., 2014; Yarnykh et al., 2015a) are also close to our measurements. Taken together, these observations confirm independence of MPF of magnetic field strength. In view of the close association between MPF and myelin content established in a number of studies (Janve et al., 2013; Ou et al., 2009; Underhill et al., 2011; Samsonov et al., 2012; Thiessen et al., 2014), field independence of MPF is especially attractive in its applications as a myelin biomarker for both human and animal studies in contrast to relaxation-based techniques (MacKay et al., 1994; Deoni et al., 2008; Hwang et al., 2010; Glasser and Van Essen, 2011) where dependence of relaxation times on the field strength may bias or hamper estimation of the myelin content.

The values of the cross-relaxation rate constant reported in the literature are characterized by rather high variability. Our measurements appear in a reasonable agreement with reference 3T data for fresh bovine brain tissues ex vivo (Stanisz et al., 2005) where k values recalculated from the reverse rate constant R were 2.2 and 2.1 s^{-1} for WM and GM, respectively. There is also good correspondence between k measured in this study and data for the canine brain at 3T (2.5 s^{-1} in WM and 1.6 s^{-1} in GM (Samsonov et al., 2012)). Higher values in ranges of 1.9–3.7 s^{-1} and 2.2–3.8 s^{-1} for WM and GM, respectively were published for the rat brain at 3T (Underhill et al., 2011). Rodent studies at high and ultra-high field strengths reported somewhat lower than our estimates: 1.3 and 0.9 s^{-1} at 7T (Thiessen et al., 2013), 1.8 and 1.4 s^{-1} at 9.4T (Xu et al., 2014), and 1.7 and 1.5 s^{-1} at 16.4T (Pohmann et al., 2011) for WM and GM, respectively. Note that the above values for 16.4T (Pohmann et al., 2011) are based on recalculation from the reverse rate constant R after averaging across anatomic regions. Human data at field strengths of 0.5T and 1.5T (Sled and Pike, 2001; Yarnykh, 2002; Sled et al., 2004; Yarnykh and Yuan, 2004; Gloor et al., 2008; Levesque et al., 2010) demonstrated consistently higher k values (up to two-fold), especially in WM. At 3T, estimates of k in the human brain based on Z-spectroscopic measurements were close to our data for GM but about 30–50% higher in WM (Underhill et al., 2009; Mossahebi et al., 2014). Notably, k values at 3T corrected for the bias caused by the effect of cross-relaxation on R_1 measurements (Mossahebi et al., 2014) appear in excellent quantitative agreement with our data for WM and slightly lower for GM. At the same time, the measurements by the on-resonance inversion recovery method (Dortch et al., 2011) at 3T yielded substantially lower k of 1.3 in WM and 1.1 s^{-1} in GM at 3T, as recalculated from the originally reported reverse rate constant. A similar approach at 7T (Dortch et al., 2013) resulted in higher and very close to each other k estimates in WM and GM of 2.5 and 2.6

s^{-1}. It is also noticeable that visual appearance of k maps in this study suggests a reduced contrast between WM and GM compared to the published example maps of the human brain in lower fields (Sled and Pike, 2001; Yarnykh, 2002; Yarnykh and Yuan, 2004; Gloor et al., 2008; Underhill et al., 2009; Yarnykh, 2012; Mossahebi et al., 2014), though such inferences may be affected by differences in the noise level and window settings. Based on these observations, one cannot exclude a magnetic field dependence of the cross-relaxation rate constant with a trend of an overall decrease and a reduction of tissue-dependent variability in high fields, similar to R_1. However, k is not theoretically expected to be field-dependent within the direct two-site magnetization exchange model, as the mechanisms contributing into this parameter, the nuclear Overhauser effect (NOE) and chemical exchange do not depend on magnetic field strength. Particularly, NOE in high fields at the slow molecular motion limit is dominated by the field-independent zero-quantum term with a negligible contribution from two-quantum transitions (Edzes and Samulski, 1978). Some spurious field effects on k may arise from the simplified nature of the pseudo-first order two-pool model and certain assumptions about R_1 of pools in Z-spectroscopic data processing. Specifically, field-dependent changes in R_1 of intermediate exchange pools not accounted in the two-pool model may affect k as an effective rate constant defined within this model. Dependence of the cross-relaxation rate constant on R_1 of extracellular water originating from the two-pool approximation of the three- and four-pool exchange models has recently been demonstrated by simulations (Li et al., 2016). Depending on the water compartmentalization scheme and a measurement technique, the trends of both decrease and increase of the measured rate constant with an increase of R_1 were predicted (Li et al., 2016). As such, multi-compartment exchange and cross-relaxation may theoretically explain possible field dependence of k or R via changes in R_1 of pools. Another source of field-dependent variability of the cross-relaxation rate constant may originate from the dipolar order effect (Morrison et al., 1995; Swanson et al., 2016; Varma et al., 2015b) neglected in the standard two-pool model. Previous studies have demonstrated that inclusion of the dipolar order reservoir into the two-pool model affects cross-relaxation rates (Morrison et al., 1995; Varma et al., 2015b), and the time constant describing dipolar order relaxation, T_{1D} may be field-dependent (Varma et al., 2015b; Varma et al., 2016). Field dependence of R_1 of the bound pool may also propagate into the measured k values, if the assumption about equality of R_1 of the pools used in the processing algorithm (Yarnykh, 2012) is violated, as suggested by some studies (Helms and Hagberg, 2009; Pohmann et al., 2011; van Gelderen et al., 2016). Finally, a slight dependence of k on magnetic field through observed R_1 may be caused by the bias due to the unaccounted effect of cross-relaxation on VFA R_1 measurements (Mossahebi et al., 2014), though correction for this bias would result in further reduction of k (Mossahebi et al., 2014). However, given high uncertainties associated with k and R estimation (Portnoy and Stanisz, 2007; Yarnykh, 2012), it is impossible to conclude at this point, whether cross-relaxation rate constants are really field-dependent. It also should be pointed out that relatively high k values were obtained on human MRI scanners with the use of off-resonance saturation techniques under specific absorption rate restrictions, which might adversely affect accuracy of k values due to insufficient saturation power (Yarnykh, 2012).

T_2^B measurements obtained in this study are highly consistent with the literature data based on the analysis with the Super-Lorentzian lineshape (Morrison and Henkelman, 1995; Sled

and Pike, 2001; Yarnykh, 2002; Sled et al., 2004; Stanisz et al, 2005; Underhill et al., 2009; Levesque et al., 2010; Pohmann et al., 2011; Underhill et al., 2011; Samsonov et al., 2012; Yarnykh, 2012; Thiessen et al., 2013; Mossahebi et al., 2014; Pampel et al., 2015; Varma et al., 2015b) and do not suggest any field dependence of this parameter. Generally, T_2^B values demonstrate minimal distinctions between WM and GM and a narrow range of variations (typically about 8–12 μs) in the brain. Residual tissue contrast on T_2^B maps has been recently attributed to the directional dependence of this parameter in WM (Yarnykh, 2012; Pampel et al., 2015). The visual appearance of T_2^B maps of the rat brain at 11.7T (Fig. 2) is in agreement with this finding, as slightly higher T_2^B values are observed in WM regions comprising fiber tracts that are known (Figini et al., 2015; Jugé et al., 2016) to run approximately parallel to the direction of the main magnetic field vector (rostral-caudal direction in Fig. 2).

Comparison of T_2 relaxation times determined from multiple spin-echoes and T_2^F measured by Z-spectroscopy in this study demonstrates close agreement between these parameters with T_2^F only slightly shorter than T_2. This finding contradicts to earlier reports for lower magnetic fields (1.5T and 3T) (Sled and Pike, 2001; Underhill et al., 2009; Levesque et al., 2010; Underhill et al., 2011) where T_2^F were approximately two-fold shorter than T_2 at corresponding field strengths. At the same time, T_2 and T_2^F appeared almost identical at 7T (Thiessen et al., 2013). Quantitative comparison of T_2^F values measured in this study with the literature (Sled and Pike, 2001; Underhill et al., 2009; Levesque et al., 2010; Underhill et al., 2011; Thiessen et al., 2013) may suggest minor magnetic field dependence for this parameter, although existing data are insufficient to substantiate this conclusion in view of different model assumptions underlying Z-spectra analysis in the above publications. Particularly, T_2^F in ranges 30–40 ms for WM and 50–55 ms for GM were reported for the human brain at 1.5T (Sled and Pike, 2001; Levesque et al., 2010). At 3T, T_2^F in the rat brain were in ranges of 27–33 ms in WM and 41–55 in GM (Underhill et al., 2011), whereas shorter values were reported for the human brain (17–27 ms in WM and 29–49 in GM (Underhill et al., 2009)). However, relatively long values of 39 and 45 ms for the corpus callosum and cortex, respectively, were found in the murine brain at 7T (Thiessen et al., 2013). As such, apparent convergence of T_2 and T_2^F values in ultra-high fields is mainly caused by shortening of the observed T_2 with an increase of the field strength, which has been noted in numerous studies (Michaeli et al., 2002; de Graaf et al., 2006; Pohmann et al., 2011; Kara et al., 2013) and appears in excellent agreement with our T_2 measurements at 11.7T. Observed trends in field-dependent discrepancies between T_2 and T_2^F support the earlier explanation (Sled and Pike, 2001) of T_2^F behavior in terms of the weighted average of multiple T_2 components corresponding to several water pools and the diffusion-mediated mechanism of T_2 shortening in high magnetic fields (Michaeli et al., 2002). Specifically, T_2^F values measured by Z-spectroscopic techniques reflect the presence of water pools with restricted mobility characterized by short T_2, which participate in the magnetization exchange with macromolecular protons and are treated collectively with free water as the free pool in the two-pool model. These short-T_2 proton populations typically belong to water immobilized within lipid bilayers of plasma membranes and/or on protein surfaces. Accordingly, they are characterized by much slower diffusion compared to free water, thus being much less affected by the dynamic dephasing on microscopic susceptibility gradients

that has been suggested as the main reason for shortening of the observed T_2 in ultra-high fields (Michaeli et al., 2002). Of note, a similar mechanism was proposed to explain discrepancies in magnetic field dependences of T_2 of spectral signals of water, metabolites, and macromolecules (de Graaf et al., 2006).

Results of this study provide validation of the fast single-point MPF mapping method with synthetic reference image (Yarnykh, 2012) for animal brain applications in ultra-high magnetic fields. This method enables the fastest possible generation of MPF maps and can be implemented with very high spatial resolution and a reasonable scan time. MPF maps obtained with the single-point method appear in excellent agreement with those reconstructed by the full fit of the two-pool model parameters. This result is similar to the findings of the earlier study (Yarnykh, 2012) where fast single-point MPF mapping was extensively validated for human brain imaging on a clinical 3T MRI scanner. Additionally, our results provide direct validation of a more time-efficient variant of the single-point method based on synthetic reference reconstruction, which has not been compared with Z-spectroscopic measurements in the initial publication (Yarnykh, 2016). The implementation of fast MPF mapping in ultra-high fields is very similar to that previously described at 3T (Yarnykh, 2012; Yarnykh, 2016), except for the constrained value of the product $R_1T_2^F$ for brain tissues, which demonstrated apparent field dependence. The value of $R_1T_2^F = 0.013$ appears about two-fold smaller than that for 3T ($R_1T_2^F = 0.022$ (Yarnykh, 2012)) mainly due to a decrease of R_1. Based on the known field-dependence of R1 (Bottomley et al., 1984; Rooney et al., 2007), the value of the product $R_1T_2^F$ can be easily estimated for implementations of the single-point reconstruction algorithm at different field strengths. The constrained value of the reverse rate constant R determined in this study (23 s^{-1}) slightly differs from that at 3T (19 s^{-1} (Yarnykh, 2012)). However, in view of large uncertainties in determination of this parameter (Portnoy and Stanisz, 2007) and low sensitivity of the signal to R at low saturation rates (Yarnykh, 2012), this difference is practically negligible, and some rounded value (for example, 20 s^{-1}) can be used as a standard constant for the single-point brain MPF mapping algorithm in a range of field strengths. Finally, due to field independence of T_2^B confirmed in this study, the standard whole-brain value of 10 μs can be used for any magnetic field.

The findings of this study may be helpful for the interpretation of contrast properties of parametric maps generated using recent semi-quantitative MT techniques, such as MTsat (Helms et al., 2008) and ihMTR (Varma et al., 2015a). Since MPF appears the main two-pool model parameter determining high-field brain tissue contrast, these techniques can be viewed as different ways to probe MPF. At the same time, effects of other two-pool model parameters may be synergistic, thus enabling additional contrast features. Particularly, a reduced inhomogeneous MT signal in muscle has been attributed to a much shorter, as compared to brain tissues, dipolar relaxation time T_{1D} (Varma et al., 2015b; Varma et al., 2016). However, this parameter appears similar in WM and GM (Varma et al., 2016) and, therefore, is unlikely to significantly contribute into the observed contrast between brain tissues. In the practical aspect, the common feature of the MTsat, ihMTR, and fast MPF mapping methods is that all of them require three source images to reconstruct corresponding maps and are capable of generating high neuroanatomical contrast in both low and high magnetic fields. An important advantage of MPF mapping is the capability of

absolute quantitation, while other techniques may benefit from simpler image processing. More research is needed to directly compare the above methods in the context of time efficiency, available spatial resolution, and image quality in structural neuroimaging applications.

This study demonstrates that fast 3D MPF mapping provides a useful approach for neuroanatomical applications in ultra-high fields where its contrast-generation capability enables excellent visualization of WM and GM structures based on differences in their myelination. An additional advantage of MPF mapping in both quantitative and structural imaging applications is its insensitivity to the presence paramagnetic ions including iron (Yarnykh, 2016). It has been demonstrated that MPF mapping improves visualization of iron-rich GM anatomical structures as compared to T_1-weighted imaging or R_1-mapping (Yarnykh, 2016) and enables unbiased iron-insensitive characterization of demyelination in subcortical GM nuclei (Krutenkova et al., 2015). Due to an increased sensitivity of high-field imaging to magnetic susceptibility effects, this feature of MPF mapping may become especially important for any high-field applications related to quantitative assessment of myelination. Another promising area of applications of high-resolution MPF mapping might include generation of anatomical templates in cell labeling and tracking studies. Most of the MRI cell-tracking techniques employ iron-oxide super-paramagnetic particles for cell labeling (Bulte et al., 2004; Lepore et al., 2006). Routinely used for neuroanatomical visualization in high fields T_2-weighted imaging is highly sensitive to the signal void effect caused by super-paramagnetic substances as well as the presence of hemorrhage after surgical procedures, which may obscure anatomical details in cell labeling applications. Since MPF mapping is based on fast gradient-echo acquisition, the signal void effect for such applications can be reduced by implementing protocols with ultra-short echo time. In combination with inherent insensitivity of MPF to the presence of paramagnetic materials, MPF mapping with ultra-short TE acquisition may become a method of choice for detailed imaging of brain anatomy before and after cell transplantation.

5. Conclusion

This study demonstrates that MPF enables the highest contrast between WM and GM in ultra-high magnetic fields as compared to other relaxation and cross-relaxation parameters. The contrast-generating capability of MPF can be exploited using the fast and robust method for 3D mapping of this parameter based on three source images, which provides a combined neuroimaging approach for both high-resolution structural imaging and quantitative tissue characterization.

Supplementary Material

Refer to Web version on PubMed Central for supplementary material.

Acknowledgments

Abbreviations

MPF	macromolecular proton fraction
MPF$_{Zsp}$	MPF maps reconstructed by the four-parameter fit of Z-spectroscopic images
MPF$_{1pt}$	MPF single-point method
MRI	magnetic resonance imaging
T	Tesla
3D	three dimensional
MT	magnetization transfer
MTR	MT ratio
MTsat	MT saturation
ihMTR	inhomogeneous MTR
PD	proton density
SNR	signal-to-noise ratio
RARE	rapid acquisition with relaxation enhancement
FSE	fast spin echo
GRE	gradient echo
TR	repetition time
TE	echo time
FOV	field of view
WM	white matter
GM	gray matter
VFA	variable flip angle
AFI	actual flip-angle imaging
ME	multi-echo
	offset frequencies
ROI	region of interest
T$_{1D}$	dipolar order longitudinal relaxation time

T_2^F	T_2 of free protons
T_2^B	T_2 of bound protons
OB	olfactory bulbs
Cg	cingulum
CC	corpus callosum
CPu	caudate putamen
ECap	left and right external capsule
ICap	internal capsule
F	fornix
SC	superior colliculus
IC	inferior colliculus
CWM	cerebellar white matter
CGM	cerebellar gray matter
Th	thalamus
H	hippocampus
Mc	motor cortex
Vc	visual cortex

References

Balchandani P, Naidich TP. Ultra-High-Field MR Neuroimaging. Am J Neuroradiol. 2015; 36:1204–1215. [PubMed: 25523591]

Boretius S, Dechent P, Frahm J, Helms G. Magnetization Transfer Mapping of Myelinated Fiber Tracts in Living Mice at 9.4 T. Proc Intl Soc Mag Reson Med. 2010:690.

Bottomley PA, Foster TH, Argersinger RE, Pfeifer LM. A review of normal tissue hydrogen NMR relaxation times and relaxation mechanisms from 1–100 MHz: dependence on tissue type, NMR frequency, temperature, species, excision, and age. Med Phys. 1984; 11:425–448. [PubMed: 6482839]

Bulte JW, Arbab AS, Douglas T, Frank JA. Preparation of Magnetically Labeled Cells for Cell Tracking by Magnetic Resonance Imaging. Methods Enzymol. 2004; 386:275–299. [PubMed: 15120257]

de Graaf RA, Brown PB, McIntyre S, Nixon TW, Behar KL, Rothman DL. High magnetic field water and metabolite proton T1 and T2 relaxation in rat brain in vivo. Magn Reson Med. 2006; 56:386–394. [PubMed: 16767752]

Deoni SCL, Rutt BK, Arun T, Pierpaoli C, Jones DK. Gleaning multicomponent T1 and T2 information from steady-state imaging data. Magn Reson Med. 2008; 60:1372–1387. [PubMed: 19025904]

Dortch RD, Li K, Gochberg DF, Welch EB, Dula AN, Tamhane AA, Gore JC, Smith SA. Quantitative magnetization transfer imaging in human brain at 3 T via selective inversion recovery. Magn Reson Med. 2011; 66:1346–1352. [PubMed: 21608030]

Dortch RD, Moore J, Li K, Jankiewicz M, Gochberg DF, Hirtle JA, Gore JC, Smith SA. Quantitative magnetization transfer imaging of human brain at 7 T. Neuroimage. 2013; 64:640–649. [PubMed: 22940589]

Dousset V, Grossman RI, Ramer KN, Schnall MD, Young LH, Gonzalez-Scarano F, Lavi E, Cohen JA. Experimental allergic encephalomyelitis and multiple sclerosis: lesion characterization with magnetization transfer imaging. Radiology. 1992; 182:483–491. [PubMed: 1732968]

Edzes HT, Samulski ET. The measurement of cross-relaxation effects in the proton NMR spin-lattice relaxation of water in biological systems: hydrated collagen and muscle. J Magn Reson. 1978; 31:207–229.

Figini M, Zucca I, Aquino D, Pennacchio P, Nava S, Di Marzio A, Preti MG, Baselli G, Spreafico R, Frassoni C. In vivo DTI tractography of the rat brain: an atlas of the main tracts in Paxinos space with histological comparison. Magn Reson Imaging. 2015; 33:296–303. [PubMed: 25482578]

Glasser MF, Van Essen DC. Mapping human cortical areas in vivo based on myelin content as revealed by T1- and T2-weighted MRI. J Neurosci. 2011; 31:11597–11616. [PubMed: 21832190]

Gloor M, Scheffler K, Bieri O. Quantitative magnetization transfer imaging using balanced SSFP. Magn Reson Med. 2008; 60:691–700. [PubMed: 18727085]

Helms G, Hagberg GE. In vivo quantification of the bound pool T1 in human white matter using the binary spin-bath model of progressive magnetization transfer saturation. Phys Med Biol. 2009; 54:N529–540. [PubMed: 19904029]

Helms G, Dathe H, Kallenberg K, Dechent P. High-resolution maps of magnetization transfer with inherent correction for RF inhomogeneity and T1 relaxation obtained from 3D FLASH MRI. Magn Reson Med 2008. 2008; 60:1396–1407.

Hwang D, Kim DH, Du YP. In vivo multi-slice mapping of myelin water content using T2* decay. Neuroimage. 2010; 52:198–204. [PubMed: 20398770]

Jugé L, Pong AC, Bongers A, Sinkus R, Bilston LE, Cheng S. Changes in Rat Brain Tissue Microstructure and Stiffness during the Development of Experimental Obstructive Hydrocephalus. PLoS One. 2016; 11:e0148652. [PubMed: 26848844]

Janve VA, Zu Z, Yao SY, Li K, Zhang FL, Wilson KJ, Ou X, Does MD, Subramaniam S, Gochberg DF. The radial diffusivity and magnetization transfer pool size ratio are sensitive markers for demyelination in a rat model of type III multiple sclerosis (MS) lesions. Neuroimage. 2013; 74:298–305. [PubMed: 23481461]

Kara F, Chen F, Ronen I, de Groot HJ, Matysik J, Alia A. In vivo measurement of transverse relaxation time in the mouse brain at 17.6 T. Magn Reson Med. 2013; 70:985–993. [PubMed: 23161407]

Krutenkova EP, Khodanovich M Yu, Bowen JD, Gangadharan B, Jung Henson LK, Mayadev A, Repovic P, Qian P, Yarnykh VL. Demyelination and iron accumulation in subcortical gray matter (GM) in multiple sclerosis (MS). Ann Neurol. 2015; 78:S65–S65.

Lepore AC, Walczak P, Rao MS, Fischer I, Bulte JW. MR imaging of lineage-restricted neural precursors following transplantation into the adult spinal cord. Exp Neurol. 2006; 201:49–59. [PubMed: 16764862]

Levesque IR, Sled JG, Narayanan S, Giacomini PS, Ribeiro LT, Arnold DL, Pike GB. Reproducibility of quantitative magnetization-transfer imaging parameters from repeated measurements. Magn Reson Med. 2010; 64:391–400. [PubMed: 20665783]

Li K, Li H, Zhang XY, Stokes AM, Jiang X, Kang H, Quarles CC, Zu Z, Gochberg DF, Gore JC, Xu J. Influence of water compartmentation and heterogeneous relaxation on quantitative magnetization transfer imaging in rodent brain tumors. Magn Reson Med. 2016; 76:635–644. [PubMed: 26375875]

Lövblad KO, Haller S, Pereira VM. Stroke: high-field magnetic resonance imaging. Neuroimaging Clin N Am. 2012; 22:191–205. [PubMed: 22548928]

MacKay A, Whittall K, Mädler J, Li D, Paty D, Graeb D. In vivo visualization of myelin water in brain by magnetic resonance. Magn Reson Med. 1994; 31:673–677. [PubMed: 8057820]

Michaeli S, Garwood M, Zhu XH, DelaBarre L, Andersen P, Adriany G, Merkle H, Ugurbil K, Chen W. Proton T2 relaxation study of water, N-acetylaspartate, and creatine in human brain using Hahn and Carr-Purcell spin echoes at 4T and 7T. Magn Reson Med. 2002; 47:629–633. [PubMed: 11948722]

Morrison C, Henkelman RM. A model for magnetization transfer in tissues. Magn Reson Med. 1995; 33:475–482. [PubMed: 7776877]

Mossahebi P, Yarnykh VL, Samsonov A. Analysis and correction of biases in cross-relaxation MRI due to biexponential longitudinal relaxation. Magn Reson Med. 2014; 71:830–838. [PubMed: 23440870]

Morrison C, Stanisz G, Henkelman RM. Modeling magnetization transfer for biological-like systems using a semi-solid pool with a super-Lorentzian lineshape and dipolar reservoir. J Magn Reson Ser B. 1995; 108:103–113. [PubMed: 7648009]

Naumova AV, Akulov AE, Khodanovich M Yu, Yarnykh VL. High-resolution three-dimensional quantitative map of the macromolecular proton fraction distribution in the normal rat brain. Data Brief. (submitted).

Ou X, Sun SW, Liang HF, Song SK, Gochberg DF. The MT pool size ratio and the DTI radial diffusivity may reflect the myelination in shiverer and control mice. NMR Biomed. 2009; 22:480–487. [PubMed: 19123230]

Pampel A, Müller DK, Anwander A, Marschner H, Möller HE. Orientation dependence of magnetization transfer parameters in human white matter. Neuroimage. 2015; 114:136–146. [PubMed: 25862261]

Petrie EC, Cross DJ, Yarnykh VL, Richards T, Martin NM, Pagulayan K, Hoff D, Hart K, Mayer C, Tarabochia M, Raskind MA, Minoshima S, Peskind ER. Neuroimaging, behavioral, and psychological sequelae of repetitive combined blast/impact mild traumatic brain injury in Iraq and Afghanistan war veterans. J Neurotrauma. 2014; 31:425–436. [PubMed: 24102309]

Prevost VH, Girard OM, Varma G, Alsop DC, Duhamel G. Minimizing the effects of magnetization transfer asymmetry on inhomogeneous magnetization transfer (ihMT) at ultra-high magnetic field (11.75 T). MAGMA. 2016; 29:699–709. [PubMed: 26762244]

Pohmann R, Shajan G, Balla DZ. Contrast at high field: relaxation times, magnetization transfer and phase in the rat brain at 16.4 T. Magn Reson Med. 2011; 66:1572–1581. [PubMed: 21671265]

Portnoy S, Stanisz GJ. Modeling pulsed magnetization transfer. Magn Reson Med. 2007; 58:144–155. [PubMed: 17659607]

Ropele S, Seifert T, Enzinger C, Fazekas F. Method for quantitative imaging of the macromolecular 1H fraction in tissues. Magn Reson Med. 2003; 49:864–871. [PubMed: 12704769]

Raya JG, Dietrich O, Horng A, Weber J, Reiser MF, Glaser C. T2 measurement in articular cartilage: impact of the fitting method on accuracy and precision at low SNR. Magn Reson Med. 2010; 63:181–193. [PubMed: 19859960]

Rooney WD, Johnson G, Li X, Cohen ER, Kim SG, Ugurbil K, Springer CS Jr. Magnetic field and tissue dependencies of human brain longitudinal 1H2O relaxation in vivo. Magn Reson Med. 2007; 57:308–318. [PubMed: 17260370]

Samsonov A, Alexander AL, Mossahebi P, Wu YC, Duncan ID, Field AS. Quantitative MR imaging of two-pool magnetization transfer model parameters in myelin mutant shaking pup. Neuroimage. 2012; 62:1390–1398. [PubMed: 22664569]

Skinner TE, Glover GH. An extended two-point Dixon algorithm for calculating separate water, fat, and B0 images. Magn Reson Med. 1997; 37:628–630. [PubMed: 9094088]

Sled JG, Levesque I, Santos AC, Francis SJ, Narayanan S, Brass SD, Arnold DL, Pike GB. Regional variations in normal brain shown by quantitative magnetization transfer imaging. Magn Reson Med. 2004; 51:299–303. [PubMed: 14755655]

Sled JG, Pike GB. Quantitative imaging of magnetization transfer exchange and relaxation properties in vivo using MRI. Magn Reson Med. 2001; 46:923–931. [PubMed: 11675644]

Stanisz GJ, Odrobina EE, Pun J, Escaravage M, Graham SJ, Bronskill MJ, Henkelman RM. T1, T2 relaxation and magnetization transfer in tissue at 3T\. Magn Reson Med. 2005; 54:507–512. [PubMed: 16086319]

Swanson SD, Malyarenko DI, Fabiilli ML, Welsh RC, Nielsen J-F, Srinivasan A. Molecular, dynamic, and structural origin of inhomogeneous magnetization transferin lipid membranes. Magn Reson Med. 2016 Epub ahead of print.

Thiessen JD, Zhang Y, Zhang H, Wang L, Buist R, Del Bigio MR, Kong J, Li XM, Martin M. Quantitative MRI and ultrastructural examination of the cuprizone mouse model of demyelination. NMR Biomed. 2013; 26:1562–1581. [PubMed: 23943390]

Ugurbil K. Magnetic resonance imaging at ultrahigh fields. IEEE Trans Biomed Eng. 2014; 61:1364–1379. [PubMed: 24686229]

Underhill HR, Rostomily RC, Mikheev AM, Yuan C, Yarnykh VL. Fast bound pool fraction imaging of the in vivo rat brain: association with myelin content and validation in the C6 glioma model. Neuroimage. 2011; 54:2052–2065. [PubMed: 21029782]

Underhill HR, Yuan C, Yarnykh VL. Direct quantitative comparison between cross-relaxation imaging and diffusion tensor imaging of the human brain at 3.0 T. Neuroimage. 2009; 47:1568–1578. [PubMed: 19500678]

van Gelderen P, Jiang X, Duyn JH. Effects of magnetization transfer on T1 contrast in human brain white matter. Neuroimage. 2016; 128:85–95. [PubMed: 26724780]

van de Ven RC, Hogers B, van den Maagdenberg AM, de Groot HJ, Ferrari MD, Frants RR, Poelmann RE, van der Weerd L, Kiihne SR. T(1) relaxation in in vivo mouse brain at ultra-high field. Magn Reson Med. 2007; 58:390–395. [PubMed: 17654587]

Varma G, Duhamel G, de Bazelaire C, Alsop DC. Magnetization transfer from inhomogeneously broadened lines: A potential marker for myelin. Magn Reson Med. 2015a; 73:614–622. [PubMed: 24604578]

Varma G, Girard OM, Prevost VH, Grant AK, Duhamel G, Alsop DC. Interpretation of magnetization transfer from inhomogeneously broadened lines (ihMT) in tissues as a dipolar order effect within motion restricted molecules. J Magn Reson. 2015b; 260:67–76. [PubMed: 26408956]

Varma G, Girard OM, Prevost VH, Grant A, Duhamel GD, Alsop DC. In vivo measurement of a new source of tissue contrast, the dipolar relaxation time, T1D, using a modified ihMT sequence. Proc Intl Soc Mag Reson Med. 2016:802.

Xu J, Li K, Zu Z, Li X, Gochberg DF, Gore JC. Quantitative magnetization transfer imaging of rodent glioma using selective inversion recovery. NMR Biomed. 2014; 27:253–260. [PubMed: 24338993]

Yarnykh VL. Pulsed Z-spectroscopic imaging of cross-relaxation parameters in tissues for human MRI: theory and clinical applications. Magn Reson Med. 2002; 47:929–939. [PubMed: 11979572]

Yarnykh VL, Yuan C. Cross-relaxation imaging reveals detailed anatomy of white matter fiber tracts in the human brain. Neuroimage. 2004; 23:409–424. [PubMed: 15325389]

Yarnykh VL. Actual flip-angle imaging in the pulsed steady state: a method for rapid three-dimensional mapping of the transmitted radiofrequency field. Magn Reson Med. 2007; 57:192–200. [PubMed: 17191242]

Yarnykh VL. Fast macromolecular proton fraction mapping from a single off-resonance magnetization transfer measurement. Magn Reson Med. 2012; 68:166–178. [PubMed: 22190042]

Yarnykh VL. Time-efficient, high-resolution, whole brain three-dimensional macromolecular proton fraction mapping. Magn Reson Med. 2016; 75:2100–2106. [PubMed: 26102097]

Yarnykh VL, Bowen JD, Samsonov A, Repovic P, Mayadev A, Qian P, Gangadharan B, Keogh BP, Maravilla KR, Jung Henson LK. Fast whole-brain three-dimensional macromolecular proton fraction mapping in multiple sclerosis. Radiology. 2015a; 274:210–220. [PubMed: 25208343]

Yarnykh VL, Tartaglione EV, Ioannou GN. Fast macromolecular proton fraction mapping of the human liver in vivo for quantitative assessment of hepatic fibrosis. NMR Biomed. 2015b; 28:1716–1725. [PubMed: 26503401]

Highlights

- Macromolecular proton fraction (MPF) mapping was used to image rat brain at 11.7T.

- MPF provided the effective source of ultra-high-field brain tissue contrast.

- Fast single-point MPF mapping method was validated for high-field MRI applications.

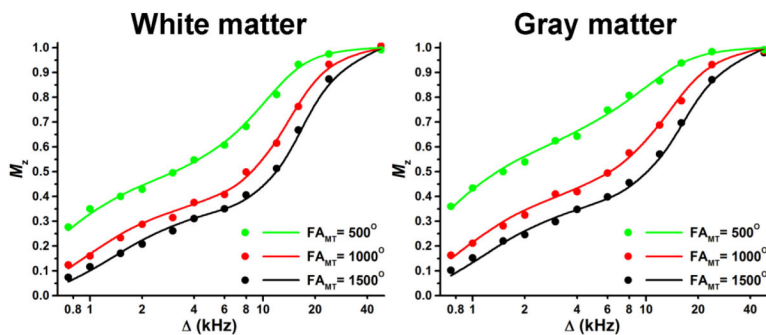- MPF mapping enables high-resolution and high-contrast imaging of brain anatomy.

Figure 1.
Experimental (points) and fitted (lines) Z-spectra in ROIs corresponding to the corpus callosum (white matter) matter and cortex (gray matter) of the rat brain obtained at the 11.7T magnetic field strength. The fitted parameters are as follows: MPF =12.9%, k=1.8 s^{-1}, T$_2^F$ = 21.9 ms, and T$_2^B$=12.0 μs for WM, and MPF = 6.1%, k=1.9 s^{-1}, T$_2^F$ = 33.3 ms, and T$_2^B$=10.0 μs for GM.
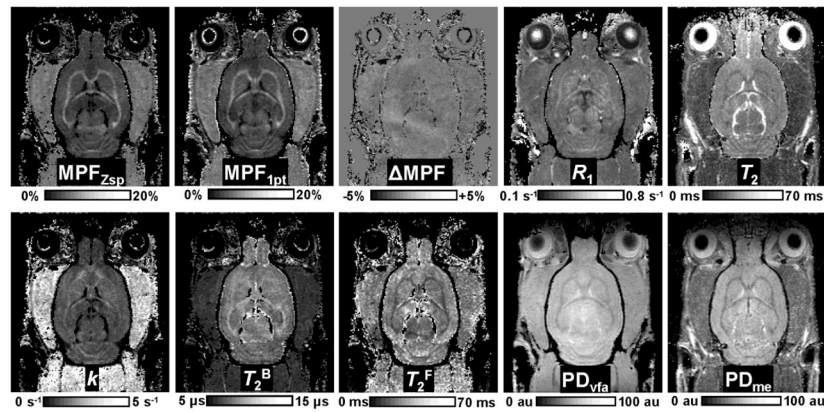
Figure 2.
Example parametric maps of the rat brain obtained at the 11.7T: MPF maps reconstructed by the four-parameter fit of Z-spectroscopic images (MPF_{Zsp}) and single-point method (MPF_{1pt}), their difference (MPF), R_1 map reconstructed from VFA data (R_1), T_2 map reconstructed from multi-echo data (T_2), maps of the cross-relaxation rate constant (k) and T_2 of the free and bound protons (T_2^F and T_2^B) obtained from the fit of Z-spectral data, and proton density maps reconstructed from VFA (PF_{vfa}) and multi-echo (PD_{me}) data. Greyscale range corresponds to the following parameter ranges: MPF_{Zsp} and MPF_{1pt}: 0–20%. MPF: $-5 - +5\%$, R_1: 0.1–0.8 s^{-1}, T_2: 0–70 ms, k: 0–5 s^{-1}, T_2^B: 5–15 µsec. and T_2^F: 0–70 ms. PD_{vfa} and PD_{me} maps are presented in arbitrary units in the range from zero to the maximal voxel intensity of cerebrospinal fluid.
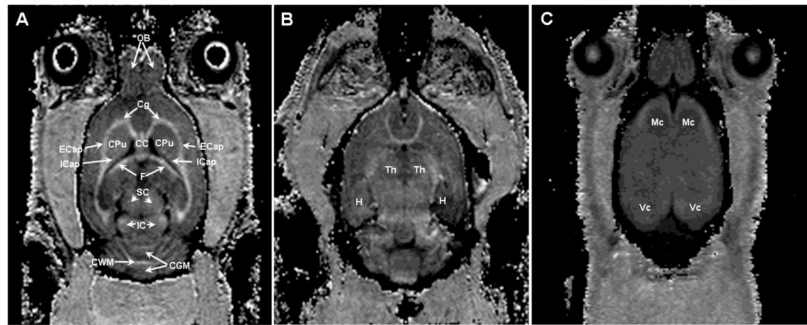
Figure 3.
Rat brain structures identified on the three coronal cross-sections (A, B, and C) of a 3D MPF map reconstructed by the single-point method. Abbreviations are as follows: OB, olfactory bulbs; Cg, cingulum; CC, corpus callosum; CPu, caudate putamen; ECap, left and right external capsule; ICap, internal capsule; F, fornix; SC, superior colliculus; IC, inferior colliculus; CWM, cerebellar white matter; CGM, cerebellar gray matter; Th, thalamus; H, hippocampus; Mc, motor cortex; Vc, visual cortex.
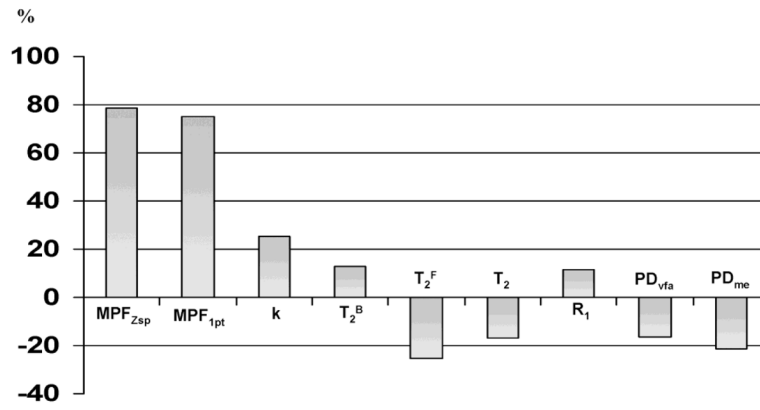
Figure 4.
Percentage difference between quantitative MRI parameters in WM and GM averaged across brain structures and reflecting tissue contrast on corresponding parametric maps.
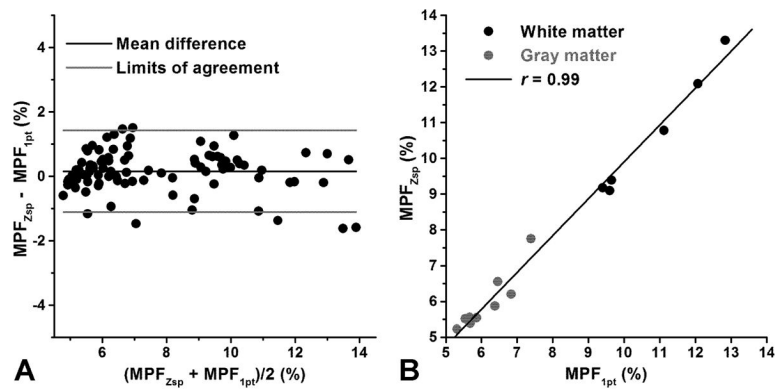
Figure 5.
Agreement between MPF measurements obtained from maps reconstructed by the four-parameter fit of Z-spectroscopic images (MPF_{Zsp}) and single-point synthetic reference method (MPF_{1p}): A: Bland-Altman plot of ROI measurements pooled across all animals and anatomic structures. Lines correspond to the mean difference (black) and limits of agreement (gray). B: Scatter plot of correlation between mean MPF measurements in brain structures with the regression line.
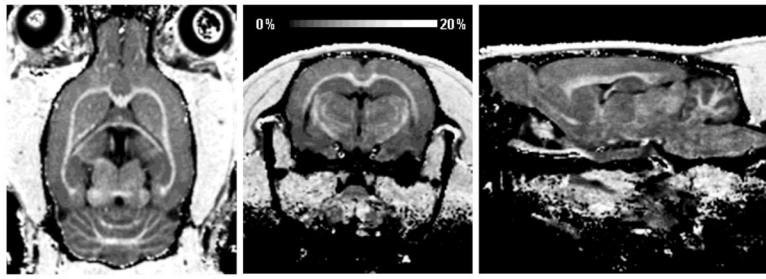
Figure 6.
Reformatted orthogonal sections of a 3D MPF map of the rat brain obtained using the single-point synthetic-reference method with isotropic resolution of 170 μm.

Table 1

Relaxation and cross-relaxation parameters in WM and GM structures of the rat brain at 11.7T.

	Brain structure	R_1, s^{-1}	T_2, ms	k, s^{-1}	T_2^{B}, μs	T_2^{F}, ms	MPF$_{Zsp}$, %	MPF$_{1pt}$, %
Gray matter	olfactory bulb	0.38±0.01	49.5±2.2	1.4±0.1	9.7±0.2	40.4±2.1	5.2 ±0.2	5.3±0.3
	caudate putamen	0.45±0.01	36.6±1.5	1.8±0.1	10.2±0.3	33.9±2.6	6.2±0.3	6.8±0.6
	hippocampus	0.39±0.02	36.2±2.7	1.5±0.1	9.6±0.7	37.7±3.1	5.6±0.4	5.7±0.6
	superior colliculus	0.47±0.02	33.4±2.2	1.5±0.1	9.9±0.6	26.6±2.1	6.6±0.4	6.5±1.1
	inferior colliculus	0.44±0.03	31.6±1.9	1.9±0.3	10.1±0.5	28.2±4.8	5.9±0.5	6.4±0.7
	cerebellar GM	0.41±0.02	35.1±1.6	1.6±0.1	9.7±0.3	39.3±7.4	5.5±0.5	5.9±0.6
	motor cortex	0.37±0.01	44.7±2.9	1.7±0.3	9.4±0.2	34.9±8.1	5.4±0.3	5.7±0.6
	visual cortex	0.37±0.02	41.1±3.3	1.7±0.1	9.5±0.3	39.2±7.0	5.5±0.4	5.6±0.5
	thalamus	0.48±0.03	32.2±1.8	1.7±0.1	10.5±0.4	26.1±3.8	7.8±1.0	7.4±1.0
	GM average	0.42±0.02	37.8±2.2	1.6±0.2	9.8±0.4	34.0±4.5	5.9±0.4	6.1±0.7
	cingulum	0.45±0.0	31.3±2.1	2.2±0.3	10.7±0.4	29.6±5.0	9.2±0.6	9.4±1.0
	corpus callosum	0.44±0.03	32.3±2.5	2.1±0.1	11.0±1.0	23.9±4.6	10.8±1.1	11.1±1.2
	external capsule	0.45±0.03	32.7±2.6	2.0±0.2	10.9±0.5	28.2±4.6	9.4±0.5	9.6±0.7
White matter	internal capsule	0.52±0.03	28.1±3.2	2.0±0.2	11.2±0.6	20.4±2.9	13.3±1.4	12.8±0.9
	fornix	0.47±0.04	33.4±1.5	1.9±0.3	11.1±0.7	27.6±2.2	9.1±0.6	9.6±0.9
	cerebellar WM	0.47±0.0	31.0±1.8	2.1±0.1	11.6±0.8	22.9±2.0	12.1±0.9	12.1±1.3
	WM average	0.47±0.03	31.5±2.38	2.0±0.2	11.1±0.7	25.4±3.6	10.7±0.9	10.7±1.0